

Synergistic photocatalytic activity of a combination of carbon nanotubes-graphene-nickel foam nanocomposites enhanced by dielectric barrier discharge plasma technology for water purification

Qihui Xu, Shuaikang Fang, Yin Chen, Jae Kwang Park, Chao Pan, Yongjun Shen, Na Zhu and Huifang Wu

ABSTRACT

Degradation activity of plasma catalysis between dielectric barrier discharge (DBD) and carbon nanotubes-graphene-nickel foam (CNTs-G-Ni_f) has been studied in treatment of dye wastewater. CNTs-G-Ni_f was prepared through a two-step chemical vapor deposition (CVD) approach. The composite has been characterized by different techniques such as X-ray diffraction (XRD), scanning electron microscope (SEM) and Raman spectroscopy. SEM results showed that the Ni_f as the growth substrate was evenly wrapped by G and then CNTs were successfully grown on G as the support. The growth mechanism of composite was proposed. The possible coupled catalytic mechanism between DBD and CNTs-G-Ni_f were addressed. In addition, the modification on G-Ni_f was found by SEM during the discharge process in liquid phase. And the modification mechanism of DBD plasma (DBDP) acting on composites was discussed. Finally, by means of analyses of ultraviolet-visible (UV-Vis) spectroscopy, Fourier transform infrared (FT-IR) spectroscopy, gas chromatography-mass spectrometry (GC-MS) and liquid chromatography-mass spectrometry (LC-MS), the general degradation pathway and stepwise degradation pathways of alizarin green (AG) were proposed in detail.

Key words | CNTs-G-Ni_f, combined system, coupling factor, DBDP catalysis, reaction mechanisms

Qihui Xu[†]
Shuaikang Fang[†]
Yin Chen[†]
Yongjun Shen (corresponding author)
Huifang Wu

School of Chemistry and Chemical Engineering,
Nantong University,
Nantong 226019,
China
E-mail: shenyj@ntu.edu.cn

Jae Kwang Park
Department of Civil and Environmental
Engineering,
University of Wisconsin–Madison,
1415 Engineering Drive,
Madison, WI 53706,
USA

Chao Pan
Yongjun Shen
Na Zhu
Nantong University Xinglin College,
Nantong 226008,
China

[†]These authors contributed equally to this work and should be considered co-first authors.

HIGHLIGHTS

- A novel degradation system DBD plasma/CNTs-G-Ni_f is proposed.
- The new model of coupling factor is put forward to evaluate the degradation effect.
- DBD plasma has modification on G-Ni_f in degradation of dye wastewater.
- Comprehensive mechanisms of preparing, coupling, modifying and degrading are explored.

INTRODUCTION

With high chroma, large displacement, high content of electrolyte and complex composition, the printing and dyeing wastewater was considered as the most pernicious industrial wastewater. Therefore, it must be thoroughly mineralized and degraded to eliminate environmental impacts (Wang

et al. 2016; Ben *et al.* 2017). Alizarin green (AG), a kind of typical anthraquinone dyes was selected as a main research object in this study. The current treatment methods for wastewater pollution mainly included physical methods, biological methods (Farabegoli *et al.* 2010), physical and chemical methods (Hayeeye *et al.* 2016; Liu *et al.* 2017), and advanced oxidation processes (AOPs). AOPs are most suitable for removing persistent and recalcitrant organic compounds. AOPs do not form harmful byproducts and

This is an Open Access article distributed under the terms of the Creative Commons Attribution Licence (CC BY 4.0), which permits copying, adaptation and redistribution, provided the original work is properly cited (<http://creativecommons.org/licenses/by/4.0/>).

doi: 10.2166/wst.2021.030

have a short reaction time because of the use of hydroxyl radicals formed by a combination of ozone (O_3), hydrogen peroxide, and ultraviolet (UV) (Colindres *et al.* 2010), Fenton's reagent (Kumar *et al.* 2011), ultrasonic (Shen *et al.* 2017a, 2017b), electrochemical oxidation (Rubi-Juarez *et al.* 2016), photocatalytic oxidation (Liu *et al.* 2006; Hou *et al.* 2019), plasma process (Jiang *et al.* 2014; Magureanu *et al.* 2015), combined technologies, etc.

It has been proven that the low temperature plasma is capable of producing a variety of highly oxidizing substances such as hydroxyl radical ($\cdot OH$), O_3 , hydrogen peroxide (H_2O_2) and superoxide radical ($\cdot O_2^-$) (Jiang *et al.* 2014). In addition, low temperature plasma also contained UV radiation, shock wave, strong electric field and pyrolysis. Therefore, low temperature plasma could be used for treating pollutants (Magureanu *et al.* 2015), especially for the refractory aromatic organics in printing and dyeing wastewater. The discharge forms of low temperature plasma mainly included pulse discharge, direct current corona discharge, glow discharge, sliding arc discharge and dielectric barrier discharge (DBD). Among these discharge forms above, low temperature plasma technology based on DBD was easy to operate and able to obtain high treatment effects. In recent years, it has received great attention in the area of water treatment (Wang *et al.* 2008; Wang *et al.* 2011; Lou *et al.* 2012; Jiang *et al.* 2016). Jiang *et al.* (Feng *et al.* 2014) reported that $250\text{ mg}\cdot\text{L}^{-1}$ of Indigo Carmine solution was completely degraded in 10 minutes at the voltage of 25 kV and frequency of 200 Hz on a dielectric barrier discharge plasma (DBDP) reactor. Compared with other AOPs, plasma technology alone showed certain superiority in degradation. However, there were still some block blanks in this field, especially in the reduction of the energy consumption and further enhancing utilization effect of the active substances in plasma system (Chen *et al.* 2009). Therefore, the combined systems of plasma have been extensively studied to solve the problems above recently, mainly including the combination with inorganic ions and various kinds of catalytic materials.

In recent years, electrode catalytic materials of carbon class (Cc) composite have been studied. A wide range of C materials included activated carbon, carbon nanotubes (CNTs), carbon nanofibers, G and various composite materials. Mousset *et al.* (2016) used different forms of G as cathode material in electro-Fenton (EF), implying the possibility of using pristine G in EF for the treatment of wastewater. Ji *et al.* (2015) demonstrated that flow-through electrode of polyaniline supported on lamellar-structured G could be used for electrocatalytic reduction of Cr^{6+} . Huang *et al.* (2013) provided a simple hydrothermal method to synthesize

wall-like layered metal oxide $MMoO_4$ ($M = Ni, Co$) nanosheet arrays, which are directly grown on flexible carbon cloth and used as a non-removal for advanced supercapacitors. Adhesive electrode. Zhang *et al.* (2016) have used a simple two-step method to fabricate $Ni_{1/3}Co_{2/3}Se_2$ nanowires and nanosheets on carbon cloth. They are interconnected to form a layered three-dimensional network structure, showing high electrochemical HER active. Vecitis *et al.* (2011) reported that active MWCNT filter was effective toward the adsorptive removal and electrochemical oxidation of the aqueous dyes, Methylene Blue and Methyl Orange, and the oxidation of the aqueous anions, chloride and iodide. Shen *et al.* (2015) confirmed that G materials could enhance the removal effect of dye, oil, organic solvents, heavy metal ions and gas pollutants. Zhang *et al.* (2010) reported that the CNTs-pillared RGO composite materials could exhibit an excellent visible light photocatalytic performance in degrading dye Rhodamine B because of the unique porous structure and the exceptional electron transfer property of G. Based on the studies above, there were reasons to consider that Cc electrode catalytic materials could also be combined with DBDP to treat wastewater on account of its unique discharge structure. Recently, (Sun *et al.* 2010) used the solid carbon source at 1,073 K to produce large, high quality and controllable G and doped G. Latorre *et al.* (2010) used phenomenological model to describe the growth process of CNTs prepared in chemical vapor deposition (CVD) method. Lv *et al.* (2014) suggested that CNTs could be combined with G to form three-dimensional (3D) structure. However, the CNTs-G- Ni_f was prepared through a two-step CVD approach with methane (CH_4) functioned as the carbon source which was distinguished from the ethanol functioned likewise (Zhu *et al.* 2014). 2D materials can be water treated through photothermal evaporation, antibacterial and photocatalysis. Therefore, research on this application is also explosive growth (Xie *et al.* 2020a, 2020b). Due to its large absorption surface, strong absorption in the broad solar spectrum and effective photothermal conversion, two-dimensional nanomaterials have attracted great attention in water production induced by photothermal evaporation. And two-dimensional photothermal materials surpassed graphene in terms of clean water production (Xie *et al.* 2020a, 2020b). However, since the band gap of the most commonly used 2D materials is not as good as 3D carriers in terms of photocatalysis (Zhang *et al.* 2019), there are certain limitations.

As a kind of fixed phase of 3D material, CNTs-G- Ni_f should be more suitable for the DBDP reaction system, compared with powder catalysts. Such CNTs-G- Ni_f was convenient for subsequent separation and cleaning. At the same time, it could be used as a pseudo electrode material

due to its special electrochemical properties. Meanwhile, DBDP could solve the problem of activation on CNTs which should be activated before used. In addition, DBDP also had modification on G and CNTs in wastewater, which was interesting to study as well. In summary, a novel degradation system, where CNTs-G-Ni_f was combined with DBDP, would be first proposed and investigated in this study. The degradation effects AG by DBDP and DBD/CNTs-G-Ni_f were evaluated with kinetics model, respectively. The growth mechanism of prepared composites, coupled with the catalytic mechanism between DBD and CNTs-G-Ni_f, and degradation mechanism of AG were explored one by one.

EXPERIMENTAL SECTION

Experimental materials

All of chemicals were of analytical grade. Polyethylene glycol (PEG, MW = 20,000), ethanol, acetone, hexamethylenetetramine, Ni(NO₃)₂·6H₂O, ZnSO₄·7H₂O, NaOH and KCl were purchased from Xilong Scientific Co., Ltd (Guangdong, China). AG and H₂SO₄ were purchased from Sinopharm Chemical Reagent Co., Ltd. The deionized water was used throughout this study.

Preparation

The Ni_f (2 cm × 2 cm, thickness 1.0 mm, 99.99% purity) was washed for several times by an ultrasonic cleaner using acetone, ethanol and distilled water, respectively. Then, the Ni_f was taken out and dried slowly. A Ni_f was placed in quartz boat (20 mm). The quartz boat was pushed into the center of a horizontal quartz tube (100 mm diameter) in a tube furnace (Anhui BEQ Equipment Technology Co., Ltd, China, Figure 1(a)), and heated to 1,273 K under mixed gas of 30 standard m²/min H₂ and 200 standard m³/min (sccm) Argon (Ar). Then, reaction gas of CH₄ was fed to the system at flow rates of 15 sccm, keeping 30 min at 1,273 K for G growth. Subsequently, the sample was rapidly cooled down to room temperature under H₂ and Ar flow, resulting in high quality G layers grown on both sides of the Ni_f. The dip-drawing method was used to coat G with a catalyst solution. The G-Ni_f substrate was dipped into 10 mL ethanol/polyethylene glycol (PEG) (10%, w/w) solution containing 0.1 mol·L⁻¹ Ni(NO₃)₂ for about 5 min, and then drawn out and dried in air slowly. Prior to the growth of CNTs, the G-Ni_f substrate was heated to 773 K for 10 min under Ar flow (170 sccm), followed by H₂ annealing (50 sccm). Then,

the furnace temperature was continued to increase to 1,173 K under Ar and H₂ flow. The CH₄ (30 sccm) mixed with Ar and H₂ was added into the tube furnace at the reaction temperature of 1,173 K for 40 min. Subsequently, the sample was cooled down to room temperature under protection of Ar flow. And the CNTs-G-Ni_f could be obtained.

Characterization

The phase and composition of the as-prepared samples were detected by X-ray diffraction (XRD) studies using an X-ray diffractometer with Cu K α radiation under 40 kV and 40 mA with ranging from 10° to 80° at a scanning rate of 10°·min⁻¹ (D/MAX-III A, Japan). Raman spectroscopy studies were carried out on a Dispersive MicroRaman spectrometer (Invia, Renishaw) with an argon-ion laser at an excitation wavelength of 514 nm in the range 500–3,000 cm⁻¹. The morphology of the prepared samples was examined using a scanning electron microscope (SEM) (Hitachi S-4700, Japan).

Degradation activities

Figure 1(b) illustrated the DBDP reactor (DBD-50, Nanjing Suman Plasma Scientific Co., Ltd). The H₂SO₄ (0.1 M) and

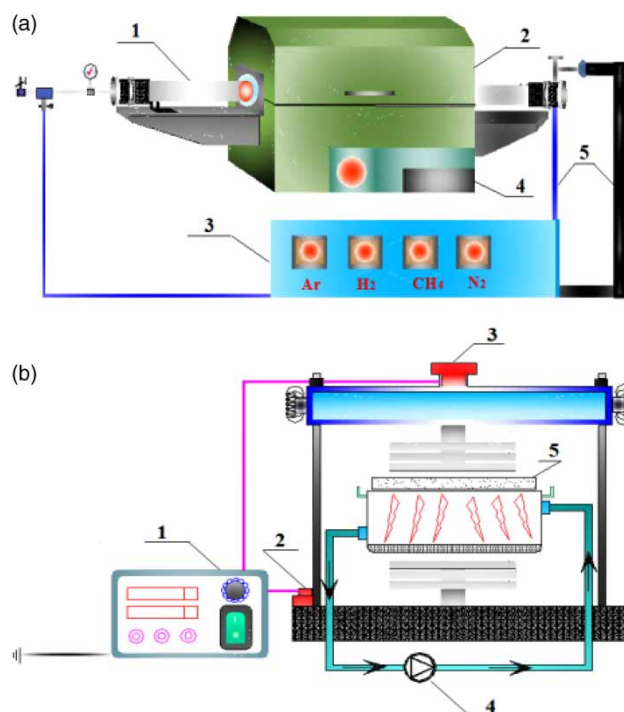


Figure 1 | CVD reaction equipment (a) (1. quartz tube, 2. tube furnace, 3. gas control valves, 4. temperature indicator, 5. breather pipe) and DBDP generator (b) (1. power source, 2. cathode interface, 3. anode interface, 4. circulating pump, 5. reaction kettle).

NaOH (0.1 M) were applied to adjust the pH of solution (pH 2.0–11.0) determined by a pH meter (pHS-25C, Shanghai Yidian Scientific Instrument Co., Ltd, China). The conductivity of solution ($105\text{--}2,000\ \mu\text{S}\cdot\text{cm}^{-1}$) was adjusted by KCl and determined using an electrical conductivity meter (DDS-307, Shanghai Yueping Scientific Instrument Co., Ltd, China). The corresponding concentrations of AG ($50\text{--}200\ \text{mg}\cdot\text{L}^{-1}$) were configured and the corresponding input powers ($56\text{--}112\ \text{W}$) were adjusted by controlling currents. Coupling system of DBDP/CNTs-G-Ni_f were operated with CNTs-G-Ni_f $2\ \text{cm}\times 2\ \text{cm}$. The absorbance of the sample was determined at regular intervals during the degradation process.

Analysis of samples

The samples were taken from the degradation process of AG under DBDP/CNTs-G-Ni_f. The UV-Vis spectrum was determined by using Shimadzu UV-1601PC UV-Vis Scanning Spectrophotometer with the wavelength ranging from 200 to 800 nm. FT-IR spectra of the samples were recorded by Tensor 27, Bruker spectrometer (Germany) over the wavelength range of $4,000\text{--}400\ \text{cm}^{-1}$. The GC-MS analysis was performed to identify the intermediates produced through the AG degradation using a method described in our previous study. Meanwhile, the samples were also analyzed by LC-MS spectrometry (Water Alliance 2795 LC) to assist the identification of degradation products.

RESULTS AND DISCUSSION

Characterization analysis

Macroscopic feature

It could be seen from Figure 2 that they were Ni_f, G-Ni_f and CNTs-G-Ni_f from left to right in order. The clean Ni_f presented silvery white and had metallic luster. After the growth of G on Ni_f, the color of composite was changed to be grey and the texture became hardened. After the growth of CNTs on G-Ni_f, the color of composite was jet black. Inverting the colors of the digital photo, some changes on the surface of Ni_f could be found after compositing G and CNTs. Black dots could be found on the surface of G-Ni_f. It could be explained that Ni may be separated out from sample during the cooling process. But few black dots could be found on the surface of CNTs-G-Ni_f, which illustrated that G-Ni_f was completely covered with CNTs.

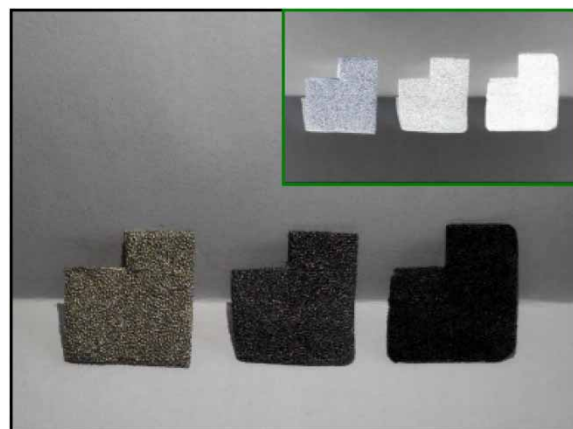


Figure 2 | The digital and colorinvert photos of Ni_f, G-Ni_f and CNTs-G-Ni_f.

Morphology and structure analysis

Figure 3 showed images of XRD and Raman in regard to CNTs-G-Ni_f. XRD spectrum depicted in Figure 3(a) showed a series of peaks. The peak (002) stood for the existence of element C while the peaks (111), (200) and (220) represented the existence of element Ni. Besides, there was no existence of other elements or oxides. This was consistent with the result that the material composition could be seen from SEM. From Figure 3(b), the existence of D-peak and 2D-peak indicated that the material had a typical graphite structure (He *et al.* 2013). 2D-peak was relatively weak, indicating the G was multilayer (Zhu *et al.* 2014). G-peak was mainly caused by the stretching vibration of C=C (sp^2) on the sheet of G. D-peak was referred to as the defect peak, which was caused by the stretching vibration of disordered or sp^3 hybridized C atoms in the carbon material, corresponding to the defect level of carbon materials (Georgakilas *et al.* 2016). The literature proved that the integrity of the composite's structure could be maintained during the growing process of G and CNTs on Ni_f (He *et al.* 2013).

Figure 4 showed the images of SEM in different growth stages of composite materials. As illustrated in Figure 4(a), the surface of Ni_f was slightly rough, but the whole was relatively smooth within $100\ \mu\text{m}$. It could be seen clearly that the surface of Ni_f substrate was encased by squamous G layers after first step CVD growth from Figure 4(b). The relative datum manifested that there were 2–5 layers G when it was grown based on Ni (Zhang *et al.* 2013). It was obvious that there were many wrinkles on G through the illustration of Figure 4(b). This was due to the inconsistent coefficient of thermal expansion between Ni_f and G (Dong *et al.* 2012a, 2012b). It could also be seen that there were some white

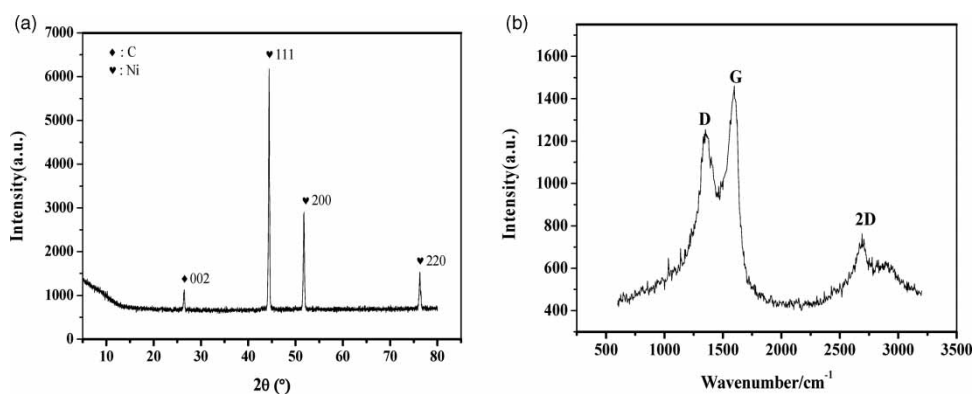


Figure 3 | The XRD (a) and Raman (b) patterns of samples.

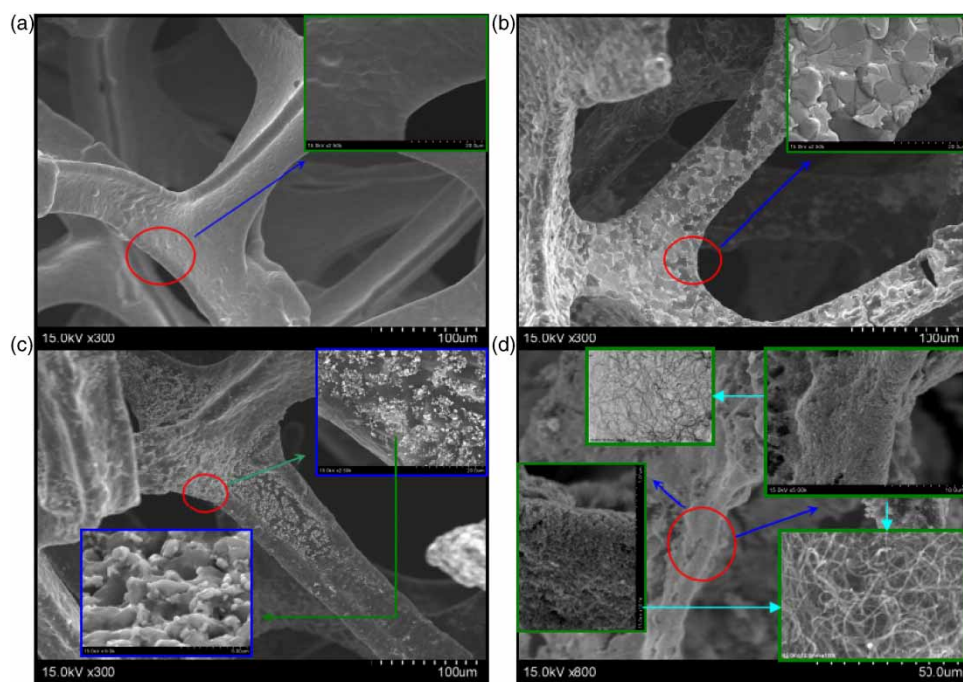


Figure 4 | The SEM photographs of samples (a) Ni; (b) G-Ni; (c) Ni crystalline-G-Ni; (d) CNTs-G-Ni.

matters on the surface of G, which may be the Ni separated out from the skeleton of Ni_f during the cooling process (Dong *et al.* 2012a, 2012b). The micro display was exactly echoed with the macro display of colorinvert photos in Figure 2. As shown in Figure 4(c), it could be found that there were thickly-dotted tiny crystals clustered on the G layer randomly. This was because that Ni salt on the surface of G layer was turned into Ni nanoparticles after high temperature with 773 K in the tube furnace, which could be the subsequent catalyst for growing CNTs (Dong *et al.* 2012a,

2012b). As shown in Figure 4(d), rough and curved CNTs were randomly grown on the surface of G after the second step of CVD growth. As can be seen from Figure 4, the whole composite maintained the honeycomb-shaped structure after repeated growth. The overall morphology of each stage was similar to that reported by the literatures (Dong *et al.* 2012a, 2012b; Zhu *et al.* 2014). This fully demonstrated that it was feasible to prepare similar products in different carbon source conditions by replacing ethanol with CH₄.

Application of DBDP alone

Effect of operational parameters

In terms of wastewater treatment with DBDP, there were many influence factors. Precisely, four common influence factors would be studied in this study, including concentration of dye, pH of solution, conductivity of solution and input power of DBDP. Figure S1 (Supplementary material) shows the changes between decolorization rate of AG and values of four factors. The decolorization rate was decreased when values of concentration, pH and conductivity were gradually increased. But the decolorization rate increased when values of input power were gradually increased. The amount of active material and high energy electron produced in plasma discharge was constant at the same time as when the input power was unchanged. When the concentration of AG was higher, the relative decolorization rate was lower. It could be found that acidic condition was of benefit to degradation of AG. The data showed that the oxidation potential of $\cdot\text{OH}$ was 2.74 eV when pH was 3 but the oxidation potential of $\cdot\text{OH}$ was only 2.34 eV when pH was 9. It illustrated that the oxidation ability of $\cdot\text{OH}$ was stronger under acidic condition (Dong et al. 2012a, 2012b). DBD was non-equilibrium discharge and the energy was transferred to other molecules through the collision so that the target could be excited or dissociated. With the increase in conductivity, the process of micro-discharge was hindered and the formation of strong reactive free radicals was slowed down, thus the degradation reaction was reduced. The increase of input power could promote the increase of energy in the reaction, which was conducive to produce more active substances and high energy electrons. Thus, the increase in input power was beneficial to the degradation of AG.

Establishment of the kinetics model equation

The reaction order showed the relationship between the concentration of the remaining reactants and the reaction rate. Through the analysis of the experimental data, the reaction order could be determined. It was demonstrated that the degradation of AG could be regarded as the pseudo-first-order reaction kinetics in DBDP alone by plotting of $\ln(c/c_0)$ - t . It can also be obtained from Figure S2 that $\ln(c/c_0)$ - t presented better linear fitting before 60 seconds. As can be seen in Table 1, the R^2 values of $\ln(c/c_0)$ - t that were greater than 0.99, 0.97 and 0.93 accounted for 45, 85 and 100% of the total R^2 values, respectively, which illustrated the degradation process of AG could be described in a first-order kinetic model in 60 seconds. When the reaction time exceeded 60 seconds, the data points started to fluctuate, and then the degradation process was no longer accurate with the first-order reaction kinetics model. It also reflected that the degradation reaction process became complicated and the large number of intermediates would be produced. Thus, the relationship between concentration of residual AG and reaction rate was affected. The degradation process of AG was an imprecise first-order reaction kinetics model when the reaction time was more than 60 seconds.

The proportionality constant of the apparent chemical reaction rate equation could be called the apparent chemical reaction rate constant. In the DBDP reaction system, the apparent chemical equation was determined as follows:

$$-\frac{dc}{dt} = k_{DBDPC} = k_{obs}c \quad (1)$$

where c is the concentration of target pollutant, k_{DBDPC} is the kinetic constant of DBDP system, k_{obs} is the apparent chemical reaction rate constant, and t is time.

Table 1 | The value of R^2 under different factors

Concentration ($\text{mg}\cdot\text{L}^{-1}$)	50	75	100	150	200	Figure S2a
R^2	0.99204	0.99669	0.97806	0.99726	0.96614	
pH	11	9	6.5	4	2	Figure S2b
R^2	0.93729	0.97557	0.99726	0.99297	0.99651	
Conductivity ($\mu\text{S}\cdot\text{cm}^{-1}$)	105	105	105	105	105	Figure S2c
R^2	0.97323	0.98248	0.98284	0.98949	0.97974	
Input power(W)	56	70	84	98	112	Figure S2d
R^2	0.94054	0.99273	0.98284	0.99461	0.99356	

There were many factors influencing the apparent reaction rate, such as concentration, temperature and pH (Beltran-Heredia et al. 2001; Gao et al. 2004; Cheng et al. 2013). Beltran-Heredia et al. (2001) used a modified Arrhenius expression to explain that the kinetic rate constants were affected by the temperature and pH. Cheng et al. (2013) showed that the kinetic constant was affected by the target concentration and ozone consumption when the light intensity was constant. The similar kinetics model equation was used to describe the degradation process by other AOPs except DBDP in our previous research (Shen et al. 2017a, 2017b).

For the study of dye wastewater treatment using plasma, concentration of AG, pH, conductivity, and the input power were selected as the factors. The following empirical model was used to describe the apparent reaction rate constant in this study:

$$k_{obs} = Ac_0^\alpha [OH^-]^\beta K_{con}^\gamma P^\varepsilon \quad (2)$$

where k_{obs} is the apparent reaction rate constant, A refers to the former factor, c_0 is the concentration of AG ($\text{mg}\cdot\text{L}^{-1}$), $[OH^-]$ is pH value, K_{con} is the solution conductivity ($\mu\text{S}\cdot\text{cm}^{-1}$), P is input power (W), and α , β , γ and ε are corresponding mathematical constants.

Equation (3) could be got by logarithm of the above equation.

$$\ln k_{obs} = \ln A + \alpha \ln c_0 + \beta \ln [OH^-] + \gamma \ln K_{con} + \varepsilon \ln P \quad (3)$$

Since the voltage in this study was set to 70 V, Equation (3) becomes:

$$\ln k_{obs} = \ln A + \alpha \ln c_0 + \beta \ln [OH^-] + \gamma \ln K_{con} + \varepsilon \ln (P/70) \quad (4)$$

Then, linear fitting of the $\ln k_{obs}$ served as function of $\ln c_0$, $\ln [OH^-]$, $\ln K_{con}$ and $\ln P$.

A multiple regression analysis of the k_{obs} value vs. c_0 , $[OH^-]$, K_{con} and P was followed, leading to: $\alpha = -0.547$, $\beta = -0.0743$, $\gamma = -0.1036$ and $\varepsilon = 2.68$ from Figure S3.

Then, the apparent reaction rate constant, k_{obs} becomes:

$$k_{obs} = Ac_0^{-0.547} [OH^-]^{-0.0743} K_{con}^{-0.104} (P/70)^{2.68} \quad (5)$$

$A = 0.681$ by calculating, Equation (5) becomes as follows:

$$k_{obs} = 0.681c_0^{-0.547} [OH^-]^{-0.0743} K_{con}^{-0.104} (P/70)^{2.68} \quad (6)$$

When Equation (6) was substituted into Equation (1), Equation (7) could be obtained:

$$c_u = c_0 \exp\{-0.681c_0^{-0.547} [OH^-]^{-0.0743} K_{con}^{-0.104} (P/70)^{2.68} t\} \quad (7)$$

where c_u was the residual amount of AG.

Equation (7) was the apparent chemical equation established for treatment process of AG wastewater under DBDP.

Application of combined systems

As shown in Figure 5, the kinetic constant of DBDP alone was 0.0179. The kinetic constant of DBDP/CNTs-G-Ni_f was namely $k_{(DBDP/CNTs-G-Ni_f)} = 0.0257$. The kinetic constant of CNTs-G-Ni_f alone $k_{(CNTs-G-Ni_f)}$ could be approximated as 0 in 150 s. Therefore, cofactor E , which was commonly used to evaluate synergistic effect of the combined system before, would be got through the Equation (8):

$$E = \frac{k_{(DBDP/CNTs-G-Ni_f)}}{k_{(DBDP)} + k_{(CNTs-G-Ni_f)}} = \frac{0.0257}{0.0179 + 0} = 1.44 \quad (8)$$

Data presentation of synergistic effect was that $1 + 1 > 2$. The cofactor $E = 1.44 > 1$ illustrated that there was synergistic effect DBDP/CNTs-G-Ni_f. This result was consistent with coupling effect.

Exploration of reaction mechanisms

The preparation mechanism on composite

In order to understand the growth of composite at various stages better, a feasible preparation mechanism was proposed by probing into the process of preparation in this study. As Figure 6 illustrated, C atoms would infiltrate into metallic Ni and the whole temporarily formed a solid solution state influenced by high temperature when CH₄ and foam nickel were used as the carbon source and the base of growth, respectively. Relevant data study indicated that the solubility of C in Ni was about 0.9% when the reaction temperature reached to 1,173 K (Li et al. 2009). Because of

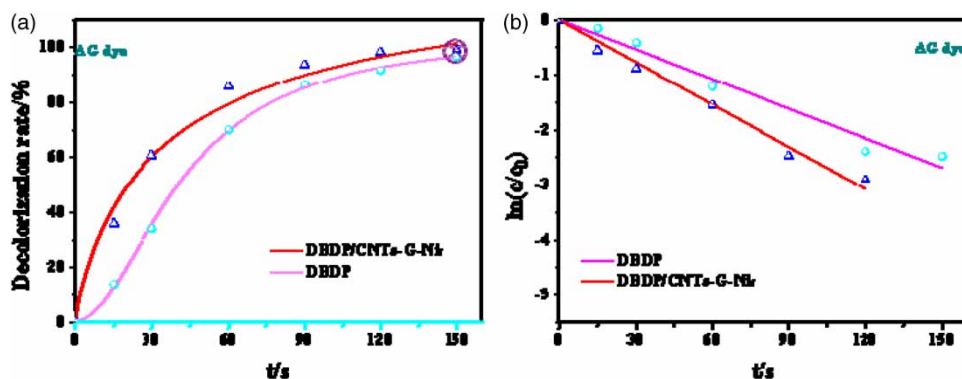


Figure 5 | The comparison analysis on combined systems: (a) decolorization rate; (b) k_{obs} .

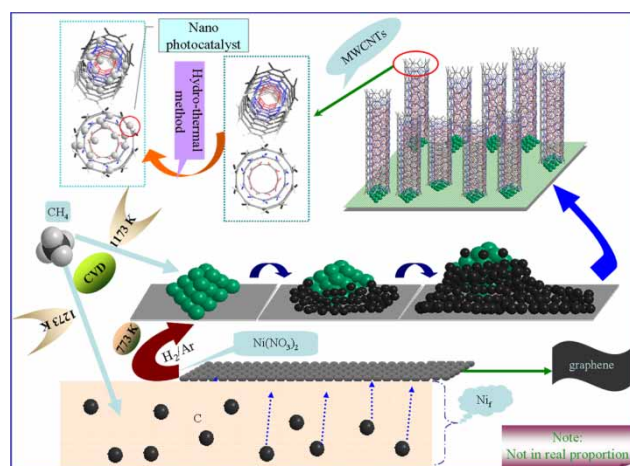


Figure 6 | The schematic illustration for preparation mechanism of the class of X-Ni_f.

the cooling effect, the oversaturated C atoms were separated out of Ni surface to form grapheme (Kim *et al.* 2009; Guermoune *et al.* 2011), namely G-Ni_f. The G-Ni_f dipped in Ni salt/ethanol/PEG solution was slowly pulled out to form coating state on its surface (Kim *et al.* 2012). Then, Ni nanoparticles, the growth catalysts of CNTs, were randomly formed on the surface of G due to the thermal expansion and H₂ etching during the process of heat treatment (Nessim *et al.* 2008). On account of subsequent high temperature, the rapid spread of C atoms piled and accumulated from the bottom of nano-Ni growth catalysts to form directional CNTs (Czekaj *et al.* 2007; Kim *et al.* 2012) which was confirmed as multi-walled CNTs (Dong *et al.* 2012a, 2012b), namely CNTs-G-Ni_f. In addition, to make a vision, the nanocatalysts with smaller size could be loaded on the surface of CNTs to form nanocatalysts-CNTs-G-Ni_f in order to further enhance the properties of composite materials.

The coupled catalytic mechanism between DBDP and CNTs-G-Ni_f

An explicable coupled catalytic mechanism was expounded in Figure 7 relying on the process of degradation treatment in this study. CNTs-G-Ni_f was located in the bottom of water phase and was separated by a layer of quartz medium with low voltage pole of DBDP. The current flowed from high voltage pole would firstly flow through CNTs-G-Ni_f then flowed to low voltage pole. Therefore, the CNTs-G-Ni_f could be regarded as the pseudo-cathode materials of DBDP, enhancing the stability of discharge and the performance of mass transfer, to improve the effect of plasma catalysis. In addition, the composite CNTs-G-Ni_f which presented the honeycomb structure on the whole could target contaminants in a relatively wide range. The CNTs grown under the support of G could

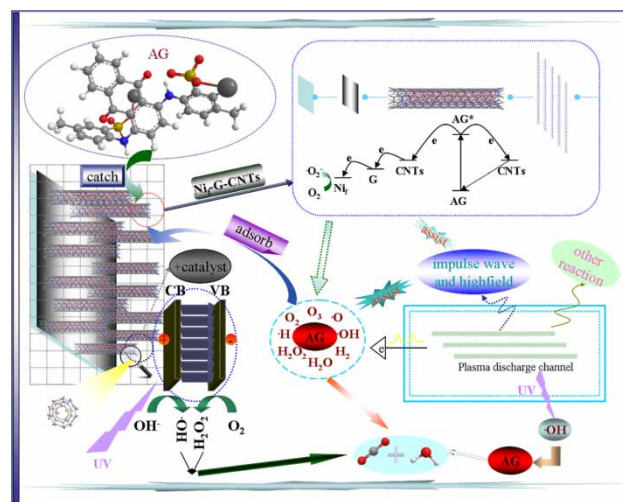


Figure 7 | The mechanism of composite materials coupled with DBDP.

lower the overpotential of the substrate in the reaction of DBDP. At the same time, CNTs as the channel of electron transport could promote electron transfer and enlarge current response (Sun et al. 2010). Thus, the special plasma catalysis effect could be produced for the mineralization of substances such as dye of AG and its degradation products.

Since CNTs had special one-dimensional hollow tubular structures and high specific surface area (Lv et al. 2014), the surface of inside and outside layer of CNTs had a lot of active points which could be regarded as host of active material generated by discharge (Sánchez-Polo et al. 2005; Valdman et al. 2018) and adsorption points which could be utilized to capture and adsorb organic contaminants in aqueous solution (Liu et al. 2013).

On account of the effect in the atmosphere of DBDP, dye molecules adsorbed on the surface of CNTs were in an excited state to originate photoinduced electron which would firstly transfer to carbon tube, and then transfer to Ni substrate step by step following energy level. O_2 in the solution or on the surface of composite material would be captured by photo-induced electron, then reduced into $\cdot O_2^-$ (Yim & Liu 2004). Thus, the efficiency of electron transfer was accelerated in reduction reaction of O_2 , which could improve the productivity of H_2O_2 . The positive hole reacted with H_2O or OH^- on the surface of the composite material, leading to generate a large amount of $\cdot OH$. Meanwhile, H_2O around the active points on the CNTs would also be more easily influenced by shock waves or strong electric fields of plasma to form $\cdot OH$ and $\cdot H$. The O_2 in the water medium could have the reaction with $\cdot H$ to form $\cdot O_2^-$ which would be converted into $\cdot OH$ and other strong oxidation free radicals through chemical reactions (Zhang et al. 2008; Gong et al. 2019). In a word, the cyclic degradation model 'adsorption capture/catalytic oxidation' was realized in DBDP/CNTs-G-Ni_f.

Degradation mechanism on intermediates and pathway of AG

Analysis of UV-Vis spectrum. Among the wave length of 200–800 nm, there were five main characteristic peaks of AG which were at 254 nm, 284 nm, 412, 606 and 644 nm, respectively. Peak at 254 nm corresponded to the absorption peak of benzene ring. Peaks at 284 and 412 nm corresponded to the absorption peaks of anthraquinone structure. Peaks at 606 and 644 nm meant that the absorption of the conjugate structure was in visible part (Xiong et al. 2013). It could be seen from Figure 8(a) that the structure of AG was very symmetrical while the conjugate effect made the color of AG green. With time, the absorption peaks gradually decreased in DBDP/CNTs-G-Ni_f system, indicating that the molecular structure was constantly opened. When the treatment time was 60 seconds, the absorption peaks of the visible part disappeared completely, indicating that large molecular structures of the solution were almost completely destroyed. When the treatment time reached 90 seconds, there were weak absorption peaks only in the ultraviolet region, indicating that organic matters with aromatic ring were almost completely oxidized. At 120 seconds, all characteristic peaks disappeared completely, indicating that the decolorization was complete without the presence of the chromophoric groups, and the macromolecule organics with the aromatic ring structures were mineralized into micro-molecule acids and other small molecule products.

Analysis of FT-IR spectrum. As could be seen from Figure 8(b), peaks near $1,500\text{ cm}^{-1}$ represented the C=C vibration absorption peak of the typical benzene ring skeleton when the sample was in absence of degradation. Usually, there were four peaks, but the four peaks

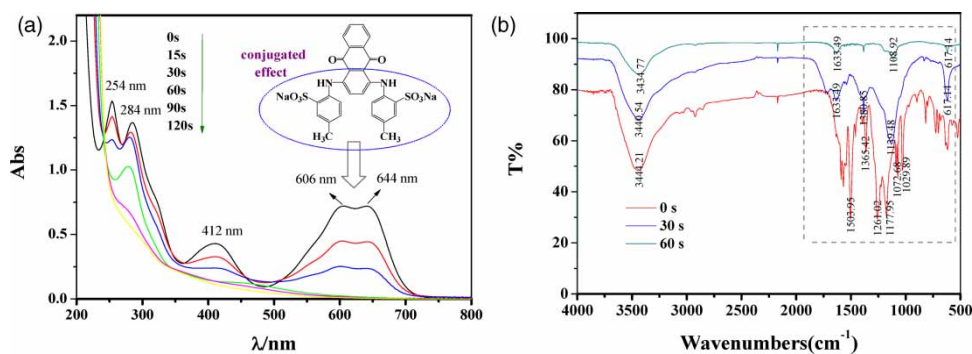


Figure 8 | The spectrum analysis of AG: (a) UV-Vis spectrum; (b) FT-IR spectroscopy.

sometimes did not appear at the same time. Peak at $1,029.89\text{ cm}^{-1}$ was the vibration absorption peak of $-\text{SO}_3\text{Na}$. Peaks at $1,261.02\text{ cm}^{-1}$ and $1,177.95\text{ cm}^{-1}$ represented the stretching vibration peak of $\text{C}=\text{O}$ in anthraquinone. Peak at $3,444.21\text{ cm}^{-1}$ represented the vibration absorption peak caused by $-\text{NH}$. The peak position of substituent group in benzene ring was at 617.14 cm^{-1} . After 30 seconds of treatment, $\text{C}=\text{C}$ vibration absorption peak of benzene ring skeleton turned into $1,633.49\text{ cm}^{-1}$, moving into takanami, which meant that original molecules with big conjugate system had become a relatively small system of benzene ring. In addition, the characteristic peak of $-\text{SO}_3\text{Na}$ disappeared. The peak of $-\text{NH}$ was transferred to $3,440.54\text{ cm}^{-1}$. Although the peak type still existed, the vibration amplitude of the peak had decreased. The peak of $\text{C}=\text{O}$ disappeared, indicating that $\text{C}=\text{O}$ had been oxidized by active substances. In terms of the dye with anthraquinone structure, the adjacent benzene rings could be oxidized and broken easily once $\text{C}=\text{O}$ was destroyed (Salazar *et al.* 2012). When the degradation time was 60 seconds, most peaks were disappeared and the remained peaks were weakened in some degree, indicating that the large molecular structure had disappeared, and the intermediate products were continuously mineralized to form small molecular products in the DBDP/CNTs-G-Ni_f system. This was consistent with the analysis of UV-Vis spectrum at 60 seconds.

Analysis of GC-MS and LC-MS spectrum. According to the analysis results of GC-MS, it could be doped out from Figure S4 that the main intermediate products were phthalic acid, hydroquinone, mesoxalic acid and various small molecular acids like acetic acid during the degradation process of AG by DBDP/CNTs-G-Ni_f. From the analysis results of LC-MS, it could be conjectured from Figure S5 that the relative molecular weights of the main intermediates existed in the degradation process of AG by DBDP/CNTs-G-Ni_f were 240, 124, 116 and 108, respectively. Through the analysis, possible intermediates were 1, 4-dihydroxyanthraquinone, 4-methyl catechol, butenedioic acid as well as p-benzoquinone, etc.

Analysis of degradation pathway. The analysis of the spectrums above, including UV-Vis, FT-IR, GC-MS and LC-MS allowed proposing a possible degradation pathway of Figure 9 for AG mineralization by DBDP/CNTs-G-Ni_f. Table 2 showed the major identified intermediates. Macromolecule of AG was broken at C-N and 1,4-dihydroxyanthraquinone (A_1) and 4-methyl catechol (C_2)

were formed after oxidation and nucleophilic reactions. The ring of A_1 would be opened through the bombardment of high-energy free radicals to form hydroquinone (A_2) and phthalic acid (A_3). The p-benzoquinone (A_4) was turned into maleic acid (A_5). Meanwhile, A_1 could be also oxidized to 1,4,9,10-anthraquinone (B_1) which was the transition state, and then A_3 and A_5 or catechol (B_4) and B_3 were formed by ring open. A_3 , B_4 , and C_2 were translated into a long chain of acids such as hexadiendioic acid and keto acid by further oxidation. Long-chain acids continued to turn into small molecular carboxylic acids such as oxalic acid (C_4), acetic acid and formic acid, which were generally reported as the end-products before totally mineralized into CO_2 and H_2O (He *et al.* 2008; Salazar *et al.* 2012).

Figure 10 explained the general sub-step pathways of degradation. As shown in S_1 , the products of two different states would be formed during the first moments of oxidation when the bonds were broken at sites 1 or 2. But $-\text{NH}_2$ could turn into $-\text{OH}$ under the function of $\cdot\text{OH}$ (He *et al.* 2008) so that the final transformations presented as A_1 and C_1 . As shown in S_2 , the phenol on the benzene ring of C_2 would be further oxidized into the ketone.

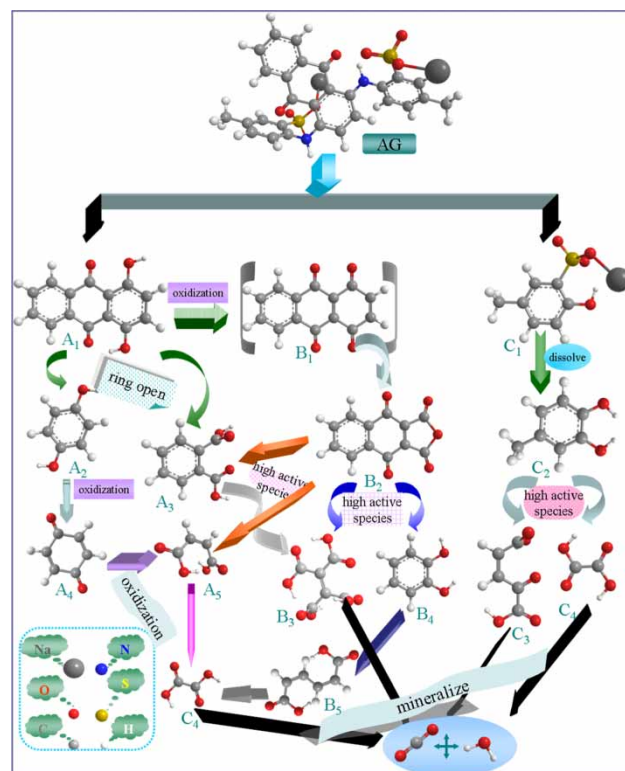
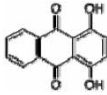
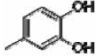
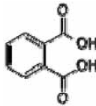
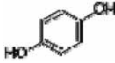
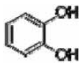
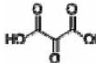
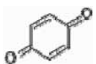
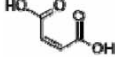
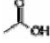


Figure 9 | The general degradation pathway of AG.

Table 2 | The determined main intermediates of AG

Number	Name	CAS number	Molecular formula	Structural formula	GC-MS/LC-MS
1	1,4-dihydroxyanthraquinone	81-64-1	C ₁₄ H ₈ O ₄		LC-MS
2	4-methyl catechol	452-86-8	C ₇ H ₈ O ₂		LC-MS
3	phthalic acid	88-99-3	C ₈ H ₆ O ₄		GC-MS R.time = 7.215 min
4	hydroquinone	123-31-9	C ₆ H ₆ O ₂		GC-MS R.time = 7.670 min
5	pyrocatechol	120-80-9	C ₆ H ₆ O ₂		GC-MS R.time = 7.670 min
6	mesoxalic acid	473-90-5	C ₃ H ₂ O ₅		GC-MS R.time = 3.705 min
7	p-benzoquinone	106-51-4	C ₆ H ₄ O ₂		LC-MS
8	butenedioic acid	110-16-7	C ₄ H ₄ O ₄		LC-MS,GC-MS R.time = 6.235 min
9	acetic acid	64-19-7	C ₂ H ₄ O ₂		GC-MS R.time = 2.035 min

Then, on the one hand, C₃ and C₄ could be formed through progressive oxidization of benzene ring. On the other hand, the methyl groups on the benzene ring could be replaced to form alcohols. The alcohols were gradually oxidized to form aldehydes and acids (Song *et al.* 2009), and then were finally converted to C₃ and C₄ by ring-open reaction.

As shown in S₅, A₁ was transformed into other intermediates by breaking bonds or further oxidation under the action of active substances. The specific transition processes of intermediate products were illustrated in Figure 11. From S₄-S₈, the oxidation transformation paths of the intermediate product in S₃ were explained in detail. In S₄, double bond was broken, ·H was transferred, and the structure was rearranged to form A₅. In S₅, 1,4-naphthoquinone through protonation and transferring of double bond was turned into 1,3-indenadione (Fanchiang & Tseng 2009; Yuan *et al.* 2011). In S₆, the ketone was decomposed into A₃ after cleavage of ring, and B₃ was formed by the further oxidation until it was mineralized to CO₂ and H₂O completely. In S₇, phenol on the benzene ring of B₄ would be

further oxidized to ketone and then oxidized to form B₅ by opening ring (Mvula & Sonntag 2003; Shen *et al.* 2016, 2017a, 2017b). In S₈, A₂ could be oxidized to A₄ (Khataee *et al.* 2016), and A₄ was finally oxidized to form A₅ due to the breakage of ring (Li *et al.* 2005).

CONCLUSIONS

Degradation process of AG could be described in a first-order kinetic model by DBDP alone within 60 seconds. It was feasible to prepare similar product CNTs-G-Ni_f using different carbon sources by replacing ethanol with methane through a two-step CVD approach. The cofactor E = 1.44 > 1 illustrated that there was synergistic effect DBDP/CNTs-G-Ni_f. The cyclic degradation model 'adsorption capture/catalytic oxidation' was realized in DBDP/CNTs-G-Ni_f. AG could be mineralized into CO₂ and H₂O by DBDP/CNTs-G-Ni_f. The results above illustrated that such CNTs-G-Ni_f

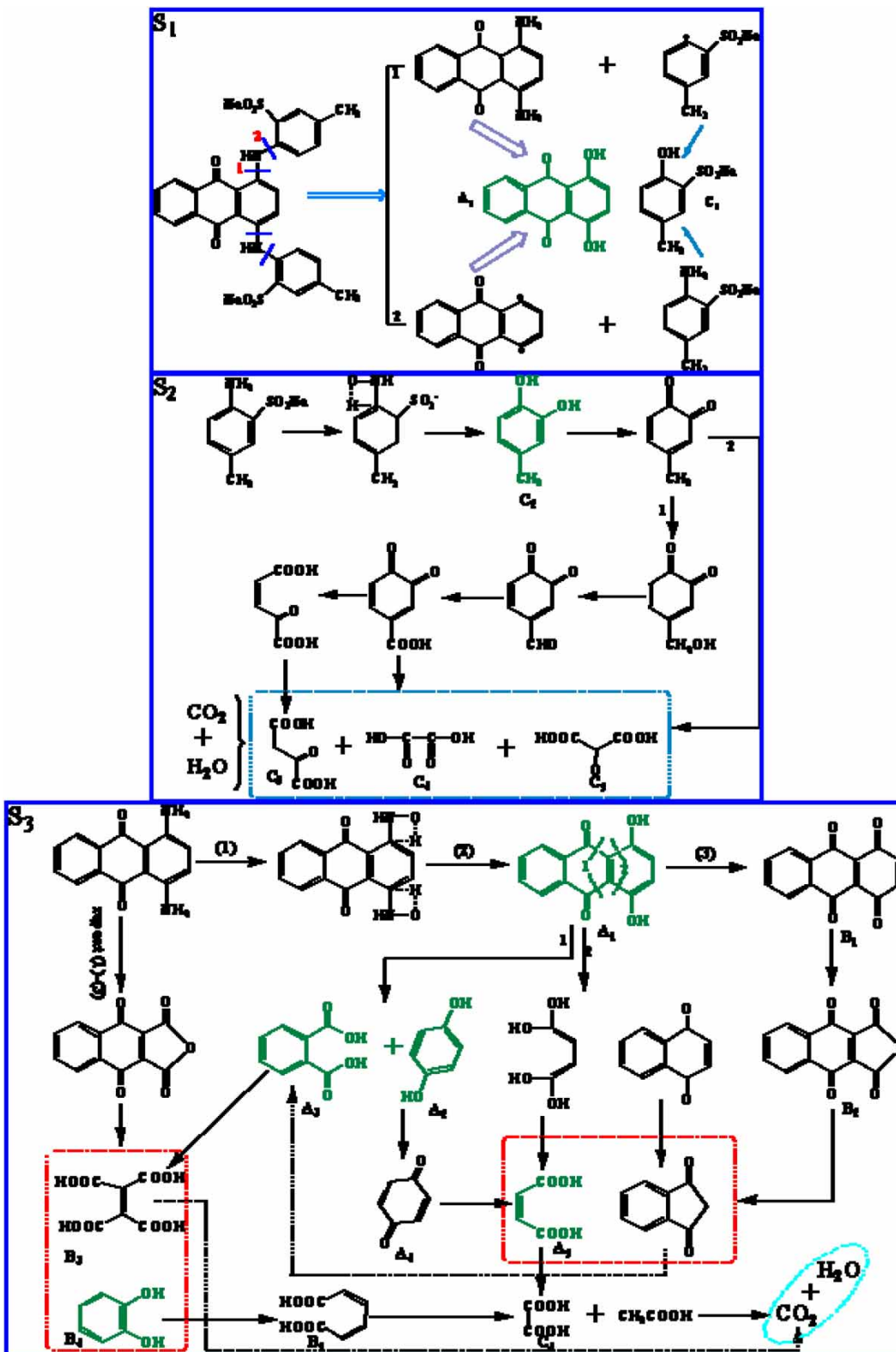


Figure 10 | The general substep degradation pathway of AG(S₁-S₃).

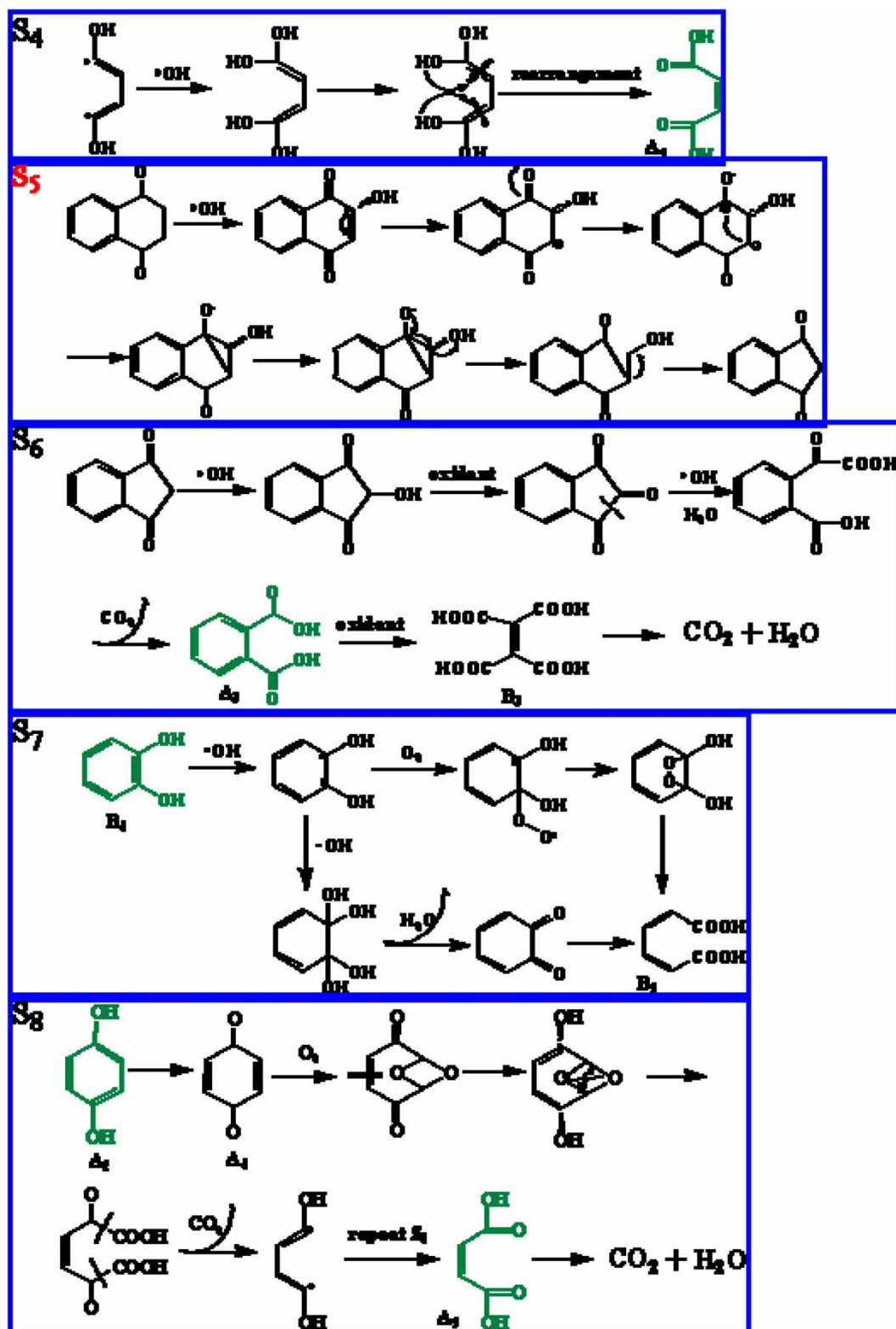


Figure 11 | The detailedly substep degradation pathway of AG(S₄-S₈).

composite represented the possibility of a new family of innovative carbon materials for plasma catalysis.

AUTHOR CONTRIBUTIONS

The manuscript was written through contributions of all authors. All authors have given approval to the final version of the manuscript.

NOTES

The authors declare no competing financial interest.

ACKNOWLEDGEMENT

The authors gratefully acknowledge the financial support from National Natural Science Foundation of China (No. 21246010).

DATA AVAILABILITY STATEMENT

All relevant data are included in the paper or its Supplementary Information.

REFERENCES

- Beltran-Heredia, J., Torregrosa, J., Dominguez, J. R. & Peres, J. A. 2001 Kinetics of the reaction between ozone and phenolic acids present in agro-industrial wastewaters. *Water Res.* **35**, 1077–1085.
- Ben, H. S., Zhao, F. P., Safaei, Z., Srivastava, V., Ramasamy, D. L., Iftekhar, S., Kalliola, S. & Sillanpaa, M. 2017 Degradation and mineralization of phenol in aqueous medium by heterogeneous monopersulfate activation on nanostructured cobalt based-perovskite catalysts ACoO₃ (A = La, Ba, Sr and Ce): characterization, kinetics and mechanism study. *Appl. Catal. B-Environ.* **215**, 60–73.
- Chen, H. L., Lee, H. M., Chen, S. H., Chang, M. B., Yu, S. J. & Li, S. N. 2009 Removal of volatile organic compounds by single-stage and two-stage plasma catalysis systems: a review of the performance enhancement mechanisms, current status, and suitable applications. *Environ. Sci. Technol.* **43**, 2216–2227.
- Cheng, Z. W., Sun, P. F., Jiang, Y. F., Yu, J. M. & Chen, J. M. 2013 Ozone-assisted UV254 nm photodegradation of gaseous ethylbenzene and chlorobenzene: effects of process parameters, degradation pathways, and kinetic analysis. *Chem. Eng. J.* **228**, 1003–1010.
- Colindres, P., Yeemadeira, H. & Reguera, E. 2010 Removal of reactive black 5 from aqueous solution by ozone for water reuse in textile dyeing processes. *Desalination.* **258**, 154–158.
- Czekaj, I., Loviat, F., Raimondi, F., Wambach, J., Biollaz, S. & Wokaun, A. 2007 Characterization of surface processes at the Ni-based catalyst during the methanation of biomass-derived synthesis gas: X-ray photoelectron spectroscopy (XPS). *Appl. Catal. A-Gen.* **329**, 68–78.
- Dong, X. C., Chen, J., Ma, Y. W., Wang, J., Chan-Park, M. B., Liu, X. M., Wang, L. H. & Huang, W. 2012a Superhydrophobic and superoleophilic hybrid foam of graphene and carbon nanotube for selective removal of oils or organic solvents from the surface of water. *P. Chen, Chem. Commun.* **48**, 10660–10662.
- Dong, X. C., Ma, Y. W., Zhu, G. Y., Huang, Y. X., Wang, J., Chan-Park, M. B., Wang, L. H., Huang, W. & Chen, P. 2012b Synthesis of graphene-carbon nanotube hybrid foam and its use as a novel three-dimensional electrode for electrochemical sensing. *J. Mater. Chem.* **22**, 17044–17048.
- Fanchiang, J. M. & Tseng, D. H. 2009 Degradation of anthraquinone dye C.I. Reactive Blue 19 in aqueous solution by ozonation. *Chemosphere* **77**, 214–221.
- Farabegoli, G., Chiavola, A., Rolle, E. & Naso, M. 2010 Decolorization of Reactive Red 195 by a mixed culture in an alternating anaerobic-aerobic Sequencing Batch Reactor. *Biochem. Eng. J.* **52**, 220–226.
- Feng, X. L., Yan, B. H., Yang, Q. L., Jin, Y. & Cheng, Y. 2014 Gas-liquid dielectric barrier discharge falling film reactor for the decoloration of dyeing water. *J. Chem. Technol. Biot.* **91**, 431–438.
- Gao, J. Z., Pu, L. M., Yang, W., Yu, J. & Li, Y. 2004 Oxidative degradation of 4-chlorophenol in aqueous induced by plasma with submersed glow discharge electrolysis. *Plasma Process. Polym.* **1**, 171–176.
- Georgakilas, V., Tiwari, J. N., Kemp, K. C., Perman, J. A., Bourlinos, A. B., Kim, K. S. & Zboril, R. 2016 Noncovalent functionalization of graphene and graphene oxide for energy materials, biosensing, catalytic, and biomedical applications. *Chem. Rev.* **116**, 5464–5519.
- Gong, B. Y., Yang, H. C., Wu, S. H., Xiong, G. P., Yan, J. H., Cen, K. F., Bo, Z. & Ostrikov, K. 2019 Graphene array-based anti-fouling solar vapour gap membrane distillation with high energy efficiency. *Nano-Micro Lett.* **11**, 2–14.
- Guermoune, A., Chari, T., Popescu, F., Sabri, S. S., Guillemette, J., Skulason, H. S., Szkopek, T. & Sij, M. 2011 Chemical vapor deposition synthesis of graphene on copper with methanol, ethanol, and propanol precursors. *Carbon.* **49**, 4204–4210.
- Hayeeye, F., Sattar, M., Chinpa, W. & Sirichote, O. 2016 Kinetics and thermodynamics of Rhodamine B adsorption by gelatin/activated carbon composite beads. *Colloid. Surface. A.* **513**, 259–266.
- He, Z. Q., Lin, L. L., Song, S., Xia, M., Xu, L. J., Ying, H. P. & Chen, J. M. 2008 Mineralization of C.I. Reactive Blue 19 by ozonation combined with sonolysis: performance optimization and degradation mechanism. *Sep. Purif. Technol.* **62**, 376–381.

- He, Y. M., Chen, W. J., Li, X. D., Zhang, Z. X., Fu, J. C., Zhao, C. H. & Xie, E. Q. 2013 Freestanding three-dimensional graphene/MnO₂ composite networks as ultra light and flexible supercapacitor electrodes. *ACS Nano* **7**, 174–182.
- Hou, L., Zhang, Y. Q., Ma, Y. Y., Wang, Y. I., Hu, Z. F., Gao, Y. Z. & Han, Z. G. 2019 Reduced phosphomolybdate hybrids as efficient visible-light photocatalysts for Cr(VI) reduction. *Inorg. Chem.* **58**, 16667–16675.
- Huang, Z. Y., Zhang, Z., Qi, X., Ren, X. H., Xu, G. H., Wan, P. B., Sun, X. M. & Zhang, H. 2013 Wall-like hierarchical metal oxide nanosheet arrays grown on carbon cloth for excellent supercapacitor electrodes. *Nanoscale*. **8**, 13273–13279.
- Ji, Q. H., Yu, D. W., Zhang, G., Lan, H. C., Liu, H. J. & Qu, J. H. 2015 Microfluidic flow through polyaniline supported by lamellar-structured graphene for mass-transfer-enhanced electrocatalytic reduction of hexavalent chromium. *Environ. Sci. Technol.* **49**, 13534–13541.
- Jiang, B., Zheng, J. T., Qiu, S., Wu, M. B., Zhang, Q. H., Yan, Z. F. & Xue, Q. Z. 2014 Review on electrical discharge plasma technology for wastewater remediation. *Chem. Eng. J.* **236**, 348–368.
- Jiang, S., Rao, J. F., Wu, Z. H. & Li, Z. 2016 Effects of coaxial dielectric barrier discharge system on water treatment by water stream well mixed with air. *IEEE T. Dielect. El. In.* **23**, 3328–3335.
- Khataee, A., Gholami, P., Vahid, B. & Joo, S. W. 2016 Heterogeneous sono-Fenton process using pyrite nanorods prepared by non-thermal plasma for degradation of an anthraquinone dye. *Ultrason. Sonochem.* **32**, 357–370.
- Kim, K. S., Zhao, Y., Jang, H., Lee, S. Y., Kim, J. M., Kim, K. S., Ahn, J. H., Kim, P., Choi, J. Y. & Hong, B. H. 2009 Centimeter scale pattern growth of graphene films for stretchable transparent electrodes. *Nature* **457**, 706–710.
- Kim, Y. S., Kumar, K., Fisher, F. T. & Yang, E. H. 2012 Out-of-plane growth of CNTs on graphene for supercapacitor applications. *Nanotechnology* **23**, 015301.
- Kumar, P., Teng, T. T., Chand, S. & Wasewar, K. L. 2011 Fenton oxidation of carpet dyeing wastewater for removal of COD and color. *Desalin. Water Treat.* **28**, 260–264.
- Latorre, N., Romeo, E., Cazana, F., Ubieta, T., Royo, C., Villacampa, J. J. & Monzon, A. 2010 Carbon nanotube growth by catalytic chemical vapor deposition: a phenomenological kinetic model. *J. Phys. Chem. C* **114**, 4773–4782.
- Li, X. Y., Cui, Y. H., Feng, Y. J., Xie, Z. M. & Gu, J. D. 2005 Reaction pathways and mechanisms of the electrochemical degradation of phenol on different electrodes. *Water Res.* **39**, 1972–1981.
- Li, X., Cai, W., Colombo, L. & Ruoff, R. S. 2009 Evolution of graphene growth on Ni and Cu by carbon isotope labeling. *Nano Lett.* **9**, 4268–4272.
- Liu, C. C., Hsieh, Y. H., Lai, P. F., Li, C. H. & Kao, C. L. 2006 Photodegradation treatment of azo dye wastewater by UV/TiO₂ process. *Dyes Pigments.* **68**, 191–195.
- Liu, X. T., Wang, M. S., Zhang, S. J. & Pan, B. C. 2013 Application potential of carbon nanotubes in water treatment: a review. *J. Environ. Sci-China.* **25**, 1263–1280.
- Liu, Y. J., Liu, J., Zhang, A. N. & Liu, Z. 2017 Treatment effects and genotoxicity relevance of the toxic organic pollutants in semi-coking wastewater by combined treatment process. *Environ. Pollut.* **220**, 13–19.
- Lou, J., Lu, N., Li, J., Wang, T. & Wu, Y. 2012 Remediation of chloramphenicol-contaminated soil by atmospheric pressure dielectric barrier discharge. *Chem. Eng. J.* **180**, 99–105.
- Lv, R., Cruz-Silva, E. & Terrones, M. 2014 Building complex hybrid carbon architectures by covalent interconnections: graphene-nanotube hybrids and more. *ACS Nano* **8**, 4061–4069.
- Magureanu, M., Mandache, N. B. & Parvulescu, V. I. 2015 Degradation of pharmaceutical compounds in water by non-thermal plasma treatment. *Water Res.* **81**, 124–136.
- Moussset, E., Wang, Z. X., Hammaker, J. & Lefebvre, O. 2016 Physico-chemical properties of pristine graphene and its performance as electrode material for electro-Fenton treatment of wastewater. *Electrochim. Acta.* **214**, 217–230.
- Mvula, E. & Sonntag, C. V. 2003 Ozonolysis of phenols in aqueous solution. *Org. Biomol. Chem.* **1**, 1749–1756.
- Nessim, G. D., Hart, A. J., Jin, S. K., Kim, J. S., Acquaviva, D., Oh, J. H., Morgan, C. D., Seita, M., Leib, J. S. & Thompson, C. V. 2008 Tuning of vertically-aligned carbon nanotube diameter and areal density through catalyst pre-treatment. *Nano Lett.* **8**, 3587–3593.
- Rubi-Juarez, H., Cotillas, S., Saez, C., Canizares, P., Barrera-Diaz, C. & Rodrigo, M. A. 2016 Removal of herbicide glyphosate by conductive-diamond electrochemical oxidation. *Appl. Catal. B-Environ.* **188**, 305–312.
- Salazar, R., Brillas, E. & Sires, I. 2012 Finding the best Fe²⁺/Cu²⁺ combination for the solar photoelectro-Fenton treatment of simulated wastewater containing the industrial textile dye disperse blue 3. *Appl. Catal. B-Environ.* **115**, 107–116.
- Sánchez-Polo, M., Von, G. U. & Rivera-Utrilla, J. 2005 Efficiency of activated carbon to transform ozone into OH radicals: influence of operational parameters. *Water Res.* **39**, 3189–3198.
- Shen, Y., Fang, Q. L. & Chen, B. L. 2015 Environmental applications of three-dimensional graphene-based macrostructures: adsorption, transformation, and detection. *Environ. Sci. Technol.* **49**, 67–84.
- Shen, Y. J., Xu, Q. H., Liang, J. & Xu, W. 2016 Degradation of Reactive Yellow X-RG by O₃/Fenton system: response surface approach, reaction mechanism, and degradation pathway. *Water Sci. Technol.* **74**, 2483–2495.
- Shen, Y. J., Xu, Q. H., Gao, D. D. & Shi, H. R. 2017a Degradation of an anthraquinone dye by ozone/Fenton: response surface approach and degradation pathway. *Ozone-Sci. Eng.* **39**, 219–232.
- Shen, Y. J., Xu, Q. H., Wei, R. R., Ma, J. L. & Wang, Y. 2017b Mechanism and dynamic study of reactive red X-3B dye degradation by ultrasonic-assisted ozone oxidation process. *Ultrason. Sonochem.* **38**, 681–692.
- Song, S., Liu, Z. W., He, Z. Q., Li, Y., Chen, J. M. & Li, C. L. 2009 Degradation of the biocide 4-chloro-3,5-dimethylphenol in aqueous medium with ozone in combination with ultraviolet

- irradiation: operating conditions influence and mechanism. *Chemosphere* **77**, 1043–1051.
- Sun, Z. Z., Yan, Z., Yao, J., Beitler, E., Zhu, Y. & Tour, J. M. 2010 Electronic transport in heterostructures of chemical vapor deposited graphene and hexagonal boron nitride. *Nature* **468**, 549–552.
- Valdman, L., Dobbs, D., Cortez, R. & Hagerman, M. E. 2018 Improving conductivity in carbon nanotube percolating networks through inclusion of Laponite nanoparticles. *Mater. Lett.* **217**, 88–91.
- Vecitis, C. D., Gao, G. D. & Liu, H. 2011 Electrochemical carbon nanotube filter for adsorption, desorption, and oxidation of aqueous dyes and anions. *J. Phys. Chem. C* **115**, 3621–3629.
- Wang, H. J., Li, J., Quan, X. & Wu, Y. 2008 Enhanced generation of oxidative species and phenol degradation in a discharge plasma system coupled with TiO₂ photocatalysis. *Appl. Catal. B-Environ.* **83**, 72–77.
- Wang, T., Lu, N., Li, J., Wu, Y. & Su, Y. 2011 Enhanced degradation of p-nitrophenol in soil in a pulsed discharge plasma-catalytic system. *J. Hazard. Mater.* **195**, 276–280.
- Wang, B., Lv, X. L., Feng, D. W., Xie, L. H., Zhang, J., Li, M., Xie, Y. B., Li, J. R. & Zhou, H. C. 2016 Highly stable Zr(IV)-based metal-organic frameworks for the detection and removal of antibiotics and organic explosives in water. *J. Am. Chem. Soc.* **138**, 6204–6216.
- Xie, Z. J., Duo, Y. H., Lin, Z. T., Fan, T. J., Xing, C. Y., Yu, L., Wang, R. H., Qiu, M., Zhang, Y. P., Zhao, Y. H., Yan, X. B. & Zhang, H. 2020a The rise of 2D photothermal materials beyond graphene for clean water production. *Adv. Sci.* **7**, 1902236.
- Xie, Z. J., Peng, Y. P., Yu, L., Xing, C. Y., Qiu, M., Hu, J. Q. & Zhang, H. 2020b Solar-Inspired water purification based on emerging 2D materials: status and challenges. *Sol. RRL* **4**, 1900400.
- Xiong, Z. D., Xu, A. H., Li, H. Y., Ruan, X. C., Xia, D. S. & Zeng, Q. F. 2013 Highly efficient photodegradation of alizarin green in TiO₂ suspensions using a microwave powered electrodeless discharged lamp. *Ind. Eng. Chem. Res.* **52**, 362–369.
- Yim, W. L. & Liu, Z. F. 2004 A reexamination of the chemisorption and desorption of ozone on the exterior of a (5,5) single-walled carbon nanotube. *Chem. Phys. Lett.* **398**, 297–303.
- Yuan, R. X., Ramjaun, S. N., Wang, Z. H. & Liu, J. S. 2011 Effects of chloride ion on degradation of acid orange 7 by sulfate radical-based advanced oxidation process: implications for formation of chlorinated aromatic compounds. *J. Hazard. Mater.* **196**, 173–179.
- Zhang, X. W., Fu, J. L. & Zhang, Y. 2008 A nitrogen functionalized carbon nanotube cathode for highly efficient electrocatalytic generation of H₂O₂ in electro-Fenton system. *Sep. Purif. Technol.* **64**, 116–123.
- Zhang, L. L., Xiong, Z. & Zhao, X. S. 2010 Pillaring chemically exfoliated graphene oxide with carbon nanotubes for photocatalytic degradation of dyes under visible light irradiation. *ACS Nano* **4**, 7030–7036.
- Zhang, Y., Zhang, L. Y. & Zhou, C. W. 2013 Review of chemical vapor deposition of graphene and related applications. *Accounts Chem. Res.* **46**, 2329–2339.
- Zhang, Z., Liu, Y. D., Ren, L., Zhang, H., Huang, Z. Y., Qi, X., Wei, X. L. & Zhong, J. X. 2016 Three-dimensional-networked Ni-Co-Se nanosheet/nanowire arrays on carbon cloth: a flexible electrode for efficient hydrogen evolution. *Electrochim. Acta.* **200**, 142–151.
- Zhang, B., Fan, T. J., Xie, N., Nie, G. H. & Zhang, H. 2019 Versatile applications of metal single-Atom @ 2D material nanoplatfoms. *Adv. Sci.* **6**, 1901787.
- Zhu, G. Y., He, Z., Chen, J., Zhao, J., Feng, X. M., Ma, Y. W., Fan, Q. L., Wang, L. H. & Huang, W. 2014 Highly conductive three-dimensional MnO₂-carbon nanotube-graphene-Ni hybrid foam as a binder-free supercapacitor electrode. *Nanoscale* **6**, 1079–1085.

First received 11 July 2020; accepted in revised form 4 January 2021. Available online 22 January 2021